A tunable polarization-independent comb filter based on high-order mode fiber

2013 J. Opt. 15 055403

(http://iopscience.iop.org/2040-8986/15/5/055403)

IOP PUBLISHING JOURNAL OF OPTICS
J. Opt. **15** (2013) 055403 (6pp) doi:10.1088/2040-8978/15/5/055403

A tunable polarization-independent comb filter based on high-order mode fiber

Chunfen Wei, Ganbin Lin, Xiaopeng Dong and Sicong Tao

Institute of Lightwave Technology, School of Information Science and Technology, Xiamen University, Xiamen 361005, People's Republic of China

E-mail: xpd@xmu.edu.cn

Received 11 November 2012, accepted for publication 27 February 2013
Published 20 March 2013
Online at stacks.iop.org/JOpt/15/055403

Abstract
This paper presents an all-fiber tunable comb filter based on high-order mode fiber (HOMF). The filter is constructed by splicing a segment of HOMF between two sections of conventional single-mode fibers (SMFs), with an intentionally introduced offset at the first joint between the SMF and HOMF, and without an offset at the second joint between the HOMF and SMF, to optimize the visibility of the transmission spectrum. The optimal transverse offset of the fibers at the first joint and the tunable polarization-independent properties of the filter were studied theoretically and experimentally. An example of using this tunable comb filter in the application of a sensor, based on demodulating the wavelength shift of a fiber Bragg grating, has also been demonstrated. The particular advantages of this all-fiber tunable filter make it valuable in various applications.

Keywords: high-order mode fiber, tunable polarization-independent filter, demodulation of a fiber Bragg grating

(Some figures may appear in colour only in the online journal)

1. Introduction

All-fiber filters are superior among optical fiber devices and sensors due to their natural compatibility with other fibers in the system. Types of all-fiber comb filters reported in the literature include (1) comb filters constructed using a Sagnac loop with a piece of highly birefringent fiber [1, 2], (2) filters with multimode fiber (MMF) [3–5], (3) filters with twin-core fiber (TCF) [6], (4) filters based on Mach–Zehnder or Michelson interferometers [7], and (5) in-line Fabry–Perot (FP) filters [8]. The filters based on mode interference by combining two beams assisted by one or two 3 dB couplers [1, 2, 7] suffer from instability and birefringence of the fiber and couplers. The interference between modes in MMF [3, 4] is difficult to manipulate because of the large number of modes in MMF. The requirement of precise alignment and cavity adjustment parts for a high-quality in-line fiber FP filter [8] makes it difficult to build and expensive in price. A filter with TCF is relatively stable and easy to tune. However, because of its asymmetrical structure in the cross-section, the filter may be subject to a polarization effect. In this paper, we propose an alternative approach to realizing a comb filter employing a piece of high-order mode fiber (HOMF), which was initially designed for dispersion compensation [9] in optical communication systems, and was used as a high-temperature sensor [10]. The principle of this HOMF filter is based on the mode interference between LP_{01} and the higher mode LP_{02}. This special filter is constructed by splicing a segment of HOMF between two sections of conventional single-mode fibers (SMF), with an intentionally introduced offset at the first joint between the SMF and HOMF, and without any offset at the second joint between the HOMF and SMF, to optimize the visibility of the transmission spectrum. The transmission spectrum of the filter is adjusted dynamically by applying longitudinal strain on the HOMF. Because of the circular symmetry in the fiber structure and field distributions of LP_{01} and LP_{02} modes, this type of filter is easy to manipulate, more stable and polarization independent.

On the basis of the performance achieved by the filter, its potential applications include fiber sensors (such as strain sensors and temperature sensors), interleavers in wavelength division multiplexing (WDM) systems, and wavelength shift demodulation, etc. As an example, utilization of this filter in the detection of a small wavelength shift of a

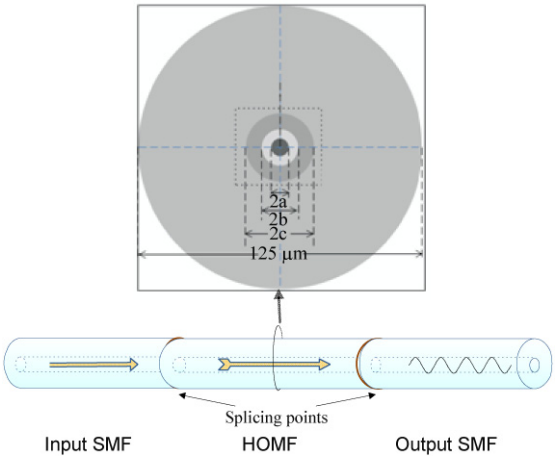

Figure 1. Schematic diagram of the HOMF filter. The inset shows the cross-section of the HOMF (a, b, and c are the radii of the inner core region, depressed index region and outer core region respectively. Here, $a = 3.86$ μm, $\Delta_1 = 2\%$, $b = 8$ μm, $\Delta_2 = -0.06\%$, $c = 15$ μm, $\Delta_3 = 0.3\%$).

fiber Bragg grating (FBG) in a displacement sensor was demonstrated. The all-fiber tunable filter that we propose has the advantages of compactness, cost-effectiveness, and polarization independence, and can be employed in various applications.

2. The design of the comb filter

The refractive index profile of the HOMF used in the experiment is specifically designed to guarantee there being only two propagating modes, i.e. the fundamental mode LP_{01} and the higher-order mode LP_{02}. The other high-order modes including LP_{11} are cut off at the operating wavelength [10–12]. The construction of the HOMF-based filter is shown in figure 1. The inset is the cross-section of the HOMF. The profile of the HOMF includes an inner core region with high relative refractive index n_1, a depressed index region with index n_2, an outer core region with index n_3, and an SiO_2 cladding with index n_{Cl}. The relative (to the cladding) index differences of each zone Δ_i are defined as $(n_i - n_{Cl})/n_{Cl}$, where $i = 1$–3. In our experiment, the radii of the inner core region, depressed index region and outer core region are 3.86 μm, 8 μm and 15 μm, respectively, and the relative index differences are $\Delta_1 = 2\%$, $\Delta_2 = -0.06\%$ and $\Delta_3 = 0.3\%$.

Because the fundamental LP_{01} mode of the input SMF at the first joint excites both LP_{01} and LP_{02} modes in the HOMF, the phase difference between these two modes is introduced after propagating over the HOMF. At the second joint, the LP_{01} and LP_{02} modes of the HOMF simultaneously launch the LP_{01} mode of the following output SMF. The optical intensity received by the output SMF after the second joint, which depends on the launching efficiency, is written as

$$I(\lambda) = I_{01} + I_{02} + 2\sqrt{I_{01}I_{02}}\cos(\Delta\varphi) \tag{1}$$

where I_{01} and I_{02} are the intensities contributed by LP_{01} and LP_{02} modes, respectively. $\Delta\varphi$ is the phase difference between the LP_{01} and LP_{02} modes in the HOMF. The phase difference $\Delta\varphi$ is given as

$$\Delta\varphi = (2\pi/\lambda)\Delta nL \tag{2}$$

where λ is the light wavelength in vacuum, Δn the difference between the effective indices of the two guided modes, and L the length of the HOMF.

In our experiments, the light source is an erbium-doped fiber amplified spontaneous emission (ASE) broadband light source pumped by a 980 nm semiconductor laser.

3. Properties of the tunable comb filter

3.1. The influence of the offset on the visibility of the transmission spectrum of the filter

With equation (1), the extinction ratio or visibility of the transmission spectrum is determined by the intensity ratio of I_{01}/I_{02}. When $I_{01}/I_{02} = 1$, the visibility reaches a maximum [13]. Therefore, to get the optimal launching efficiency of the LP_{01} and LP_{02} modes in the HOMF, an appropriate transverse offset needs to be introduced at the first joint. The launching efficiency is then calculated by using the following integral given in [14]:

$$\eta = \frac{\left|\iint_s E_i E_r^* \,\mathrm{d}s\right|^2}{\iint_s |E_i|^2 \,\mathrm{d}s \iint_s |E_r|^2 \,\mathrm{d}s} \tag{3}$$

where E_i and E_r are the fields of the excited mode and received mode, respectively.

We calculated the integral in equation (3) by setting the parameters of SMF and HOMF as follows: SMF with the core diameter of 8.3 μm, the core–cladding index difference of 0.36% (step-index profile); HOMF with the inner core region $a = 3.86$ μm, $\Delta_1 = 2\%$, the depressed index region $b = 8$ μm, $\Delta_2 = -0.06\%$, and the outer core region $c = 15$ μm, $\Delta_3 = 0.3\%$ (see figure 1). The operating wavelength is 1550 nm.

The calculated results for $(|I_{01} - I_{02}|)/(I_{01} + I_{02})$ (defined as the normalized light intensity difference) versus the transverse offset d are illustrated in figure 2. To verify the theoretical prediction, experimentally measured transmission spectra of ~20 cm HOMFs with different offsets have been shown in the insets of figure 2. The theoretical and experimental results agree well, and with the offset ~8 μm the optimal visibility of the spectrum is obtained. Moreover, in our ~20 cm HOMF case with ~8 μm offset, the full width at half-maximum (FWHM) of every single peak is ~2.09 nm, and the free spectral range (FSR) is ~4.59 nm.

3.2. The influence of the HOMF length on the FSR of the spectrum

It is clear from equation (2) that the FSR ($\Delta\lambda$) is inversely proportional to the length of the HOMF and it is calculated by using [10]

$$\Delta\lambda = \lambda_0^2/\Delta nL \tag{4}$$

where λ_0 is the central wavelength, i.e. 1550 nm.

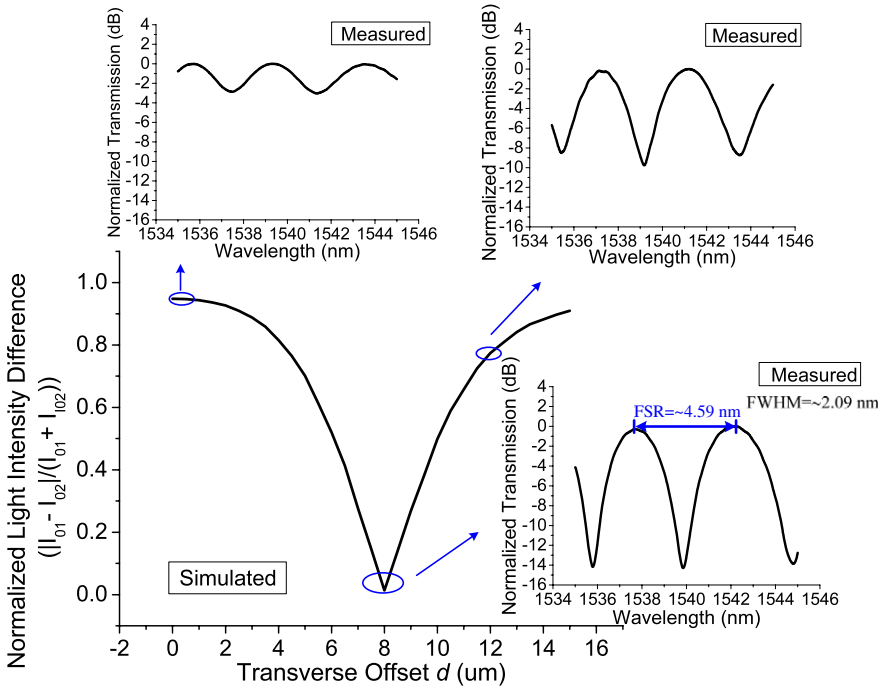

Figure 2. $(|I_{01} - I_{02}|)/(I_{01} + I_{02})$ versus the transverse offset d. The insets show the experimentally measured normalized transmission spectra of ~20 cm HOMFs with different offsets.

Figure 3 reveals the comparison of the experimental and theoretical FSRs around 1550 nm with different lengths of HOMFs (the transverse offsets are ~8 μm). It is clearly observed that the measured results almost coincide with the theoretical results.

Therefore, the FSR of the comb-like spectrum is easily adjusted by changing the length of the HOMF in the experiment. This ease of adjustment provides great flexibility and convenience in the design of the HOMF-based filter, for use in various applications with different spectrum ranges and sensitivity requirements.

3.3. The influence of the axial tension on the HOMF

The length and mode effective index are changed simultaneously when a longitudinal strain is applied to the HOMF. The corresponding change in the phase difference given in equation (2) is written as [15]

$$\frac{\partial(\Delta\varphi)}{\partial L} = \beta_1 - \beta_2 + \frac{k_0^2}{2\beta_1\beta_2}\left\{\delta[n_{\mathrm{cl}}^4(\beta_1 - \beta_2) + (n_{\mathrm{co}}^4 - n_{\mathrm{cl}}^4)(\beta_1 b_2 - \beta_2 b_1)] + V\gamma\left(\beta_1\frac{\partial b_1}{\partial V} - \beta_2\frac{\partial b_2}{\partial V}\right)\right\} \quad (5)$$

where $\delta = p_{12} - \mu(p_{11} + p_{12})$, $\gamma = \mu(n_{\mathrm{co}}^2 - n_{\mathrm{cl}}^2) + \delta(n_{\mathrm{co}}^4 - n_{\mathrm{cl}}^4)/2$, p_{11} and p_{12} are the photoelastic constants (0.12 and 0.27, respectively, for fused silica), μ is Poisson's ratio, $n_{\mathrm{co}}, n_{\mathrm{cl}}$ represent the refractive indices of the core and cladding, β_1 and β_2 represent the propagation constants of the LP_{01} and LP_{02} modes, respectively, and k_0 is the free space wavenumber. b_1 and b_2 are the normalized propagation constants of the two modes, and V is the normalized frequency. The values of $\partial b_1/\partial V$ and $\partial b_2/\partial V$ are calculated from the relation between b and V [16].

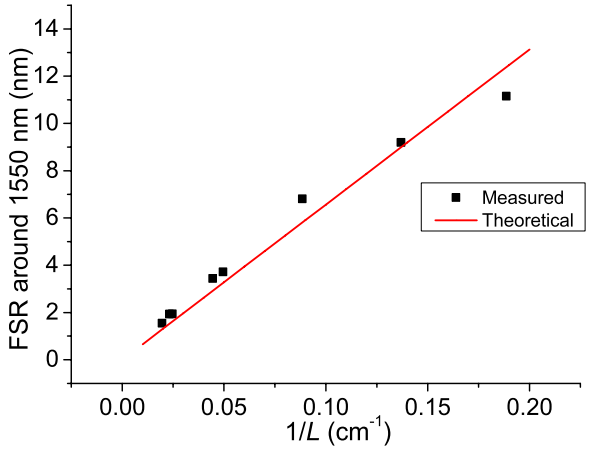

Figure 3. The comparison of the experimental and theoretical FSRs around 1550 nm with different lengths of HOMFs with the transverse offsets $d \sim 8$ μm.

With equations (1) and (5), changes of the characteristics of the comb filter under axial tension are obtained.

A piece of HOMF, ~20 cm in length, was used in the experiment to demonstrate the influence of the axial tension on the transmission spectrum. The HOMF was spliced between two SMFs as described in section 3.1 (the transverse offset was ~8 μm). To apply tension to the HOMF, one end of the HOMF was fixed to a stage and the other end was glued on a translation stage. The experimental setup is illustrated in figure 4(a). The measured spectra of the filter before and

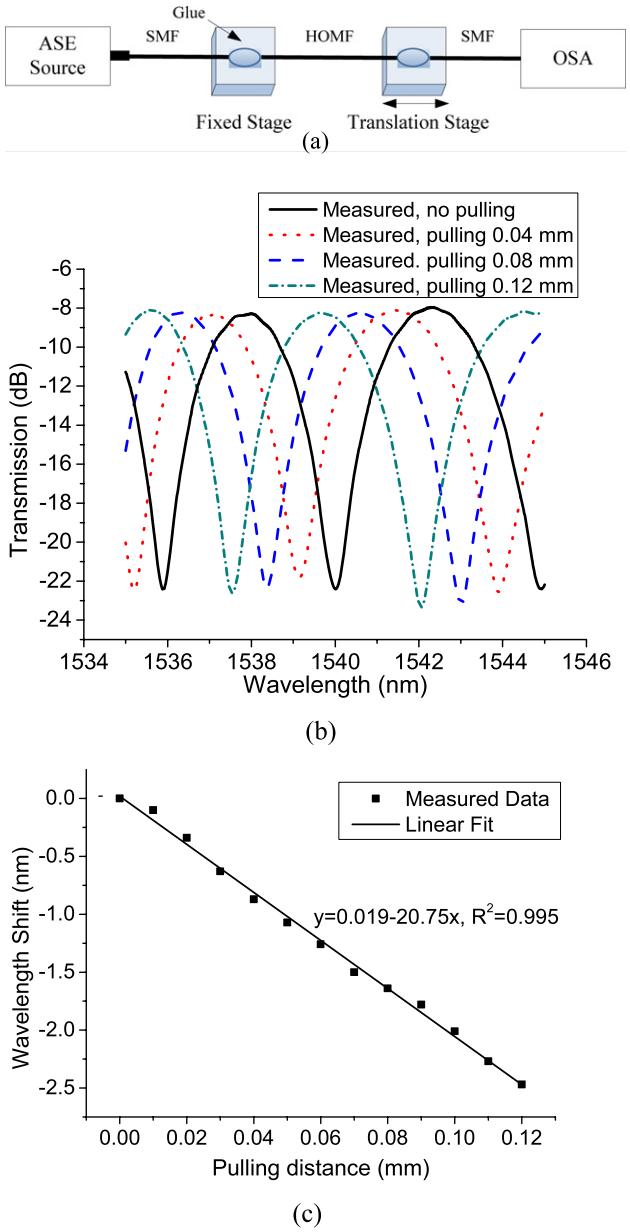

Figure 4. Influence of axial tension on the transmission spectrum. (a) Experimental setup. (b) Measured transmission spectrum. (c) Wavelength shift versus pulling distance. Here, the HOMF length L is ∼20 cm and the transverse offset d is ∼8 μm.

after pulling the HOMF 0.04 mm, 0.08 mm, and 0.12 mm are shown in figure 4(b). The spectrum shifts toward short wavelength as the pulling distance increases, and a phase change of approximately $\pi/2$ is achieved when the pulling distance is 0.12 mm. The measured relation between the wavelength shift and pulling distance is plotted in figure 4(c) with a nearly linear slope of ∼20.75 nm mm^{-1} around the wavelength of 1540 nm. Here, it should be stressed that within the axial tension limitation for the fiber, the tension-induced FSR difference is negligible.

In summary, by introducing a transverse offset between the input SMF and HOMF cores at the first joint when fusion splicing, a relatively high extinction ratio of the transmission spectrum is achieved, and by pulling the HOMF, the spectrum is dynamically tuned to meet the practical requirements.

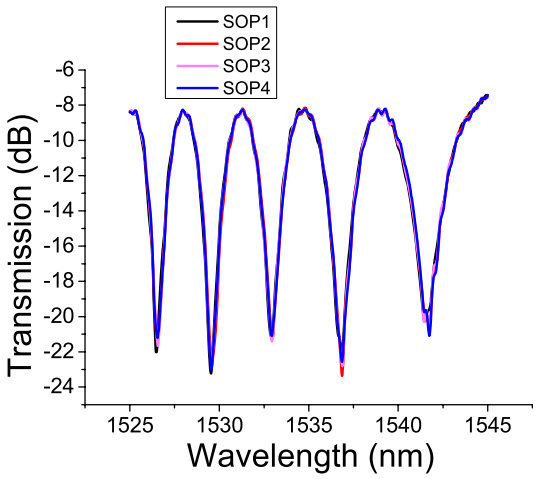

Figure 5. Transmission spectra of the filter in four SOPs of the input light (with an ∼21 cm HOMF and the transverse offset $d \sim 8$ μm).

3.4. The influence of the states of polarization (SOP) on the transmission spectrum of the filter

The stability and polarization dependence of the HOMF-based filter (with a ∼21 cm HOMF and the transverse offset ∼8 μm) are tested by launching polarized light into the fiber. A fiber pigtailed polarizer was connected to the ASE light source used in the experiment, and the input SMF of the filter was rotated to adjust the azimuth angle of the input linear polarized light. As shown in figure 5, there are almost no notable changes in the transmission spectra when changing the SOP of the input light, which shows the polarization independence of the filter.

4. Demodulation of the fiber Bragg grating wavelength shift

On the basis of the above analyses, the filter was adopted experimentally to detect tiny wavelength shifts of an FBG displacement sensor, thus verifying the feasibility of this HOMF-based demodulation scheme. The experimental arrangement is shown in figure 6. One end of the FBG was bonded to a fixed stage while the other was connected to a translation stage with a precision of 0.01 mm. By moving the translation stage to induce displacement, a longitudinal strain was introduced into the FBG. The reflected light, containing the displacement information, passed through an optical circulator to the cascaded HOMF. Then the optical intensity of the output light was measured by an optical power meter (OPM, DVP-2002A) with a resolution of 0.01 dB m.

The central wavelength and 3 dB bandwidth of the FBG are 1540.103 nm and 0.176 nm, respectively. The FBG reflects a certain quasi-single wavelength containing the displacement information.

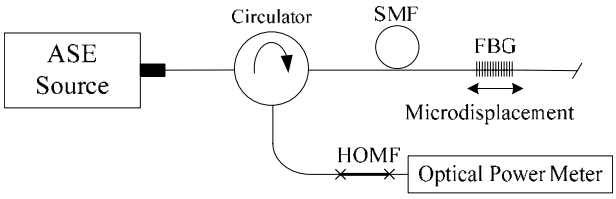

Figure 6. Experimental arrangement of the demodulating wavelength shift of an FBG displacement sensor.

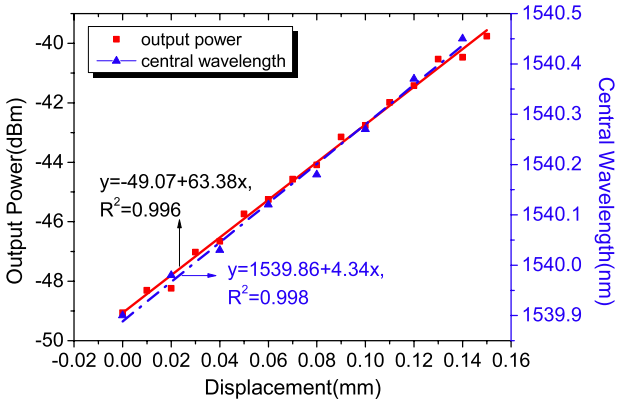

Figure 7. The dashed line corresponds to experimental measurements of the FBG displacement sensor with the OSA and the solid line corresponds to experimental results for the output demodulation intensity with displacement.

For comparison, a measurement of the FBG displacement sensor was made ahead using the optical spectrum analyzer (OSA, ANDO AQ6317B). The response of the Bragg wavelength shift is almost linear with the displacement, and the sensitivity is ∼4.34 nm mm^{-1}, as denoted by the dashed line in figure 7. Since the designed displacement range is 0.15 mm, the corresponding wavelength shift of the FBG is ∼0.65 nm, and the FSR should be no less than 1.3 nm. According to the relationship between the FSR and the length of the HOMF, the selected HOMF should be shorter than 50.5 cm. Therefore, we chose a 20 cm HOMF with the transverse offset of ∼8μm. After pulling the HOMF, we obtained a transmission spectrum with an extinction ratio of 15 dB, wavelength spacing of ∼0.7 nm and good linearity around 1540.103 nm, which offers a sufficient quasi-linear range.

The solid line in figure 7 presents the changes of intensity caused by the wavelength shift when increasing displacements up to 0.15 mm. As shown, an almost linear response is observed throughout the measured region with a high sensitivity of ∼63.38 dB m mm^{-1}. We estimate the resolution of our FBG displacement sensing system as resolution = (measured displacement range/intensity variation range) × resolution of the detector. Therefore, this displacement sensor with a HOMF-based demodulator has a resolution of ∼0.162 μm (minimum detectable displacement). Thus the corresponding minimum detectable wavelength shift is calculated to be ∼0.66 pm. In contrast, the resolution of OSA is 10 pm. Hence, our scheme exhibits great advantages in microdetection. The accuracy of this system is ±5%, due to the nonlinearity of the filter edge and the uncertainty of the OPM measurement.

As the measured displacement range is limited by the wavelength spacing of the filter, one can change to a shorter HOMF to obtain a larger wavelength spacing. However the sensitivity will decrease. There is a trade-off between the measurement range and the sensitivity of the system in the design of the demodulation filter. Despite the maximum 0.15 mm displacement measurement, the applications of the HOMF-based demodulation filter are not restricted. On cascading a spring to the FBG, the measurement range will increase [6].

Finally, we would like to make some comments on the temperature effect of the particular filter. Experiments indicated a blue shift of the spectrum with a sensitivity of 0.102 nm °C^{-1} on increasing the temperature. Therefore, the ambient temperature should be controlled when the device is applied as a demodulator.

5. Conclusions

An all-fiber tunable polarization-independent comb filter was constructed by combining a piece of HOMF between two pieces of SMF with a specific offset at the first joint. By pulling the HOMF, the spectrum of the filter was adjusted dynamically. The utility of using this type of filter in the demodulation of an FBG was demonstrated. The advantages of the tunable filter are all-fiber construction, compactness, cost-effectiveness, polarization independence, etc, making it attractive for use in various prospective devices and sensor applications.

Acknowledgment

Financial support under grant No. 61077031 from the National Natural Science Foundation of China is gratefully acknowledged.

References

[1] Fang X J and Claus R O 1995 Polarization-independent all-fiber wavelength-division multiplexer based on a Sagnac interferometer *Opt. Lett.* **20** 2146–8
[2] Dong X P, Chu B C B, Yi B and Chiang K S 2001 Novel method for the demodulation of wavelength shift of fiber Bragg gratings *Proc. SPIE* **4579** 184–7
[3] Kumar A, Varshney R K, C S A and Sharma P 2003 Transmission characteristics of SMS fiber optic sensor structures *Opt. Commun.* **219** 215–9
[4] Mehta A, Mohammed W and Johnson E G 2003 Multimode interference-based fiber-optic displacement sensor *IEEE Photon. Technol. Lett.* **15** 1129–31
[5] Liu Y and Wei L 2007 Low-cost high-sensitivity strain and temperature sensing using graded-index multimode fibers *Appl. Opt.* **46** 2516–9
[6] Zou Y, Dong X P, Lin G B and Adhami R 2012 Wide range FBG displacement sensor based on twin-core fiber filter *Lightwave Technol.* **30** 337–43
[7] Agrawal G P 1992 *Fiber-Optic Communication Systems* (New York: Wiley) pp 339–44

[8] Stone J and Stulz L W 1987 Pigtailed high-finesse tunable fiber Fabry–Perot interferometers with large, medium and small free spectral ranges *Electron. Lett.* **23** 781–3
[9] Thyagarajan K, Varshney R K, Palai P, Ghatak A K and Goyal I C 1996 A novel design of a dispersion compensating fiber *IEEE Photon. Technol. Lett.* **8** 1510–2
[10] Li Q, Lin C H, Tseng P Y and Lee H P 2005 Demonstration of high extinction ratio modal interference in a two-mode fiber and its applications for all-fiber comb filter and high-temperature sensor *Opt. Commun.* **250** 280–5
[11] Lin G B, Dong X P and Su J 2010 Design and analysis of the high-order mode dispersion compensating fiber *Proc. SPIE* **7986** 798618
[12] Lin G B and Dong X P 2012 Design of broadband $LP_{01} \leftrightarrow LP_{02}$ mode converter based on special dual-core for dispersion compensation *Appl. Opt.* **51** 4388–93
[13] Born M and Wolf E 1999 *Principles of Optics* (Cambridge: Cambridge University Press) p 289
[14] Syms R and Cozens J 1992 *Optical Guide Waves and Devices* (London: McGraw-Hill) pp 198–203
[15] Kumar A, Goel N K and Varshney R K 2001 Studies on a few-mode fiber-optic strain sensor based on LP_{01}–LP_{02} mode interference *Lightwave Technol.* **19** 358–62
[16] Okamoto K 2006 *Fundamentals of Optical Waveguides* (London: Elsevier Academic) pp 75–8